Mössbauer-NMR double resonance

M. Lippmaa, I. Tittonen,* J. Lindén, and T. Katila
Department of Technical Physics, Helsinki University of Technology, FIN-02150 Espoo, Finland
(Received 5 May 1995; revised manuscript received 19 June 1995)

We report Mössbauer measurements of $^{57}Fe_{18}Ni_{82}$ permalloy under the influence of an external radio-frequency (rf) magnetic field. Measurements were performed in both energy and time domain. Line splitting caused by direct coupling of the rf field to the nuclear spin manifolds was seen in the energy domain measurements. First observations of the time development of Mössbauer absorption in ^{57}Fe under rf magnetic excitation at specific constant Doppler velocities were also made. A $\pi/2$ phase change was observed in the absorption time dependence when measurements were performed on opposite slopes of a Mössbauer resonance line. A maximum frequency limit, above which the sample foil no longer exhibited a coherent response to the rf excitation, was observed. We also present a detailed description of an application of the density matrix theory to the analysis of the Mössbauer spectra.

I. INTRODUCTION

We have reported earlier results of Mössbauer-NMR double resonance experiments where the influence of a radio-frequency (rf) magnetic field on the Mössbauer spectrum of a thin FeNi foil was studied.[1] This work extends the previous measurement techniques into time domain and includes a more detailed analysis of the energy domain experimental results. We also show how to apply the density matrix formalism to the specific case of ^{57}Fe double resonance.

The possibility of improving the resolution of Mössbauer spectroscopy by double resonance techniques was recognized soon after the discovery of the Mössbauer effect. Early theoretical work on rf magnetic modulation in Mössbauer spectroscopy was done by Hack and Hamermesh.[2] They showed that if the rf field is in resonance with the Zeeman substates of a nuclear level, the absorption or emission lines split into $2j + 1$ components, with j being the spin of the nuclear energy level. The magnitude of the splitting depends on the amplitude of the rf field. The relative amplitudes of the component lines depend strongly on the detuning from a nuclear resonance frequency. The theory was further developed by Mitin[3] and Gabriel.[4] They analyzed the case of a rotating magnetic field coupling to either the excited or the ground state of the nucleus, including all Zeeman substates. They used the rotating wave approximation (RWA) for the rf field and could thus calculate the Mössbauer line shapes close to the nuclear resonance frequencies.

The theory has also been analyzed from the point of view of multiphoton transitions involving γ rays and photons from the rf field.[5,6] Olariu *et al.*[7] have also studied the intensity of sidebands to the otherwise forbidden transitions in an ^{57}Fe spectrum. Another, somewhat simplified description for Mössbauer-NMR double resonance has recently been published by Odeurs,[8] using the concept of dressed nuclear states.

A more general approach has been developed by Stenholm and Valli.[9–11] They solved the time dependence of the density matrix describing the nuclear system, using a continued fractions technique familiar from the work of Autler and Townes.[12] They did not need to use the RWA for the rf field, and could include phenomena like Bloch-Siegert shifts[13,14] and simultaneous coupling of the rf field to both nuclear energy levels. The theory was further adapted for Mössbauer spectroscopy by Salkola.[15] This theory is also used in our work, and presented here for the specific case of ^{57}Fe, including the absorber properties and the experimental rf field configurations. We also show that an important advantage of the theory is the capability of analyzing the time dependence of the rf modulated Mössbauer absorption.

The first experimental results on Mössbauer-NMR double resonance were obtained by Perlow[16] and Matthias.[17] The idea was to use a ferromagnetic sample in which a weak external rf field could be used to drive the much larger internal magnetization of the sample, producing a very large effective rf field amplitude seen by the Fe nuclei. Matthias observed a change in absorption in an iron foil at frequencies corresponding to the excited and ground state resonance frequencies. These changes were attributed to changes of the absorption line shape of the iron foil due to the Mössbauer-NMR resonance effects. The proof, however, was not unambiguous and Perlow argued that the changes could occur due to domain wall motion in the sample or due to acoustic modulation effects, caused by magnetostriction. These effects can give rise to prominent acoustic sidebands in a Mössbauer spectrum and have been extensively studied.[18–20] Unwanted mechanical modulation can be avoided by using nonferromagnetic materials. There have been a number of attempts to observe line splitting in nonmagnetic samples.[21–23] In these experiments, however, it has been difficult to achieve sufficient rf field amplitudes, and only sidebands and line broadening have been observed.

Significant advances have recently been made in the

0163-1829/95/52(14)/10268(10)/$06.00

use of the ^{57}Fe isotope, as has been reported by Vagizov[24,25] and in Ref. 1. Acoustic effects can be decreased or eliminated by using very thin foils and mechanical damping,[25] or by selecting a sample with an inherently small coefficient of magnetostriction.

II. THEORY

Our theoretical treatment of the ^{57}Fe double resonance phenomena uses the semiclassical density matrix approach originally developed by Stenholm.[9–11] The discrete nuclear energy levels are handled quantum mechanically, while the rf field is treated as a classical field. This theory was developed further for the specific case of rf magnetic modulation of Mössbauer transitions by Salkola and Stenholm.[15] A review of the theory is given here, adapted to the case of ^{57}Fe, and with special attention being payed to the application of the theory in the analysis of experimental data.

The quantization axis z of the nuclear system is assumed to coincide with the direction of the constant hyperfine magnetic field B_0 at the ^{57}Fe nucleus. The Hamiltonian of the system has the form

$$H = \hbar \begin{pmatrix} H_e & \mathcal{D} \\ \mathcal{D}^\dagger & H_g \end{pmatrix} + \hbar \begin{pmatrix} V_e & 0 \\ 0 & V_g \end{pmatrix} \cos(\omega t). \tag{1}$$

The first term gives the static splitting of the unperturbed two-level nuclear system and the second term describes the time-dependent interaction of the nucleus with the external harmonic magnetic field. The magnetic field frequency is ω. The two block matrices, V_e and V_g, include the coupling between the rf field and the excited and ground states of the nucleus. The excited state Hamiltonian H_e and the ground state Hamiltonian H_g are given by $H_e = \Delta_0 + \Delta_e I_{e,z}$, and $H_g = \Delta_g I_{g,z}$ with $I_{k,z}$ being the spin operator. In case of ^{57}Fe these diagonal matrices have the form

$$H_e = \begin{pmatrix} \Delta_0 + \frac{3}{2}\Delta_e & 0 & 0 & 0 \\ 0 & \Delta_0 + \frac{1}{2}\Delta_e & 0 & 0 \\ 0 & 0 & \Delta_0 - \frac{1}{2}\Delta_e & 0 \\ 0 & 0 & 0 & \Delta_0 - \frac{3}{2}\Delta_e \end{pmatrix} \tag{2}$$

and

$$H_g = \begin{pmatrix} \frac{1}{2}\Delta_g & 0 \\ 0 & -\frac{1}{2}\Delta_g \end{pmatrix}. \tag{3}$$

The energy shift between the source and the absorber is given by Δ_0. This includes the isomer shift and the Doppler shift added by the Mössbauer drive. The coupling constant is $\Delta_k = -\mu_k B_0/(I_k\hbar)$, with $k = e, g$. The constant magnetic field (typically the hyperfine field) is given by B_0, μ_k is the nuclear magnetic moment, and I_k is the nuclear spin. The magnetic field is given in Teslas, and μ_k includes the nuclear magneton. All elements of the above matrices are thus in units of angular frequency. The $\mathcal{D}$ matrix contains the transition probabilities between the different nuclear energy levels. In further calculations we actually only need products of the various matrix elements of $\mathcal{D}$ and its conjugate $\mathcal{D}^\dagger$. It is convenient to define an 8×8 matrix $\mathbf{T}$ as

$$\begin{aligned} \mathbf{T}_{ij} &= \langle I_e m_e|\mathcal{D}|I_g m_g\rangle\langle I_g m_g'|\mathcal{D}^\dagger|I_e m_e'\rangle \\ &\propto \sum_{\substack{MM' \\ q=\pm 1}} \langle I_g L m_g M|I_e m_e\rangle\langle I_g L m_g' M'|I_e m_e'\rangle \\ &\quad \times D^{(L)}_{Mq}(\phi\theta 0)[D^{(L)}_{M'q}(\phi\theta 0)]^*, \\ i &= \frac{9}{2} + 4m_g + m_e, \quad j = \frac{9}{2} + 4m_g' + m_e'. \end{aligned} \tag{4}$$

Here $\langle I_g L m_g M|I_e m_e\rangle$ is the Clebsch-Gordan coefficient, with $L = 1$, and $D^{(L)}_{Mq}(\phi\theta 0)$ is the rotation matrix. The nonzero Clebsch-Gordan coefficients are

$$\begin{aligned} \langle \tfrac{1}{2}\ 1; \pm\tfrac{1}{2}\ \ \pm 1|\tfrac{3}{2}\ \ \pm\tfrac{3}{2}\rangle &= 1, \\ \langle \tfrac{1}{2}\ 1; \pm\tfrac{1}{2}\ \ \ \ 0|\tfrac{3}{2}\ \ \pm\tfrac{1}{2}\rangle &= \sqrt{\tfrac{2}{3}}, \\ \langle \tfrac{1}{2}\ 1; \pm\tfrac{1}{2}\ \ \mp 1|\tfrac{3}{2}\ \ \mp\tfrac{1}{2}\rangle &= \sqrt{\tfrac{1}{3}}. \end{aligned} \tag{5}$$

The necessary rotation matrix elements are given by $D^{(L)}_{Mq}(\phi\theta 0) = e^{-iM\phi} d_{Mq}(\theta)$, where

$$\begin{aligned} d_{0,0} &= \cos\theta, \\ d_{\pm 1,0} &= -d_{0,\pm 1} = \mp\frac{1}{\sqrt{2}}\sin\theta, \\ d_{\mp 1,1} &= d_{\pm 1,-1} = \frac{1}{2}(1 \mp \cos\theta). \end{aligned} \tag{6}$$

The Euler angles ϕ and θ define the direction of the γ rays as shown in Fig. 1. The rf field vector $\vec{B}_{\rm rf}$ is assumed to lie in the xz plane with B_x giving the transverse and B_z the longitudinal component.

The time-dependent part of the Hamiltonian includes the interaction matrices V_e and V_g, given by $V_k = \alpha_k I_{k,x} + \beta_k I_{k,z}$, $(k = e, g)$. The coupling constants are $\alpha_k = -\mu_k B_x/(I_k\hbar)$ and $\beta_k = -\mu_k B_z/(I_k\hbar)$. The splitting of nuclear levels is affected by β_k, which is proportional to the longitudinal rf field component, and only appears on the diagonal of the interaction matrix. The coupling constant α_k is proportional to the I_x spin opera-

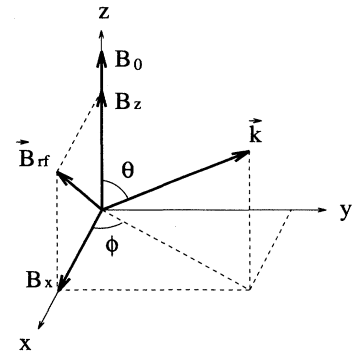

FIG. 1. Direction of the static field B_0, γ rays $\vec{k}$, and the rf magnetic field $\vec{B}_{\rm rf}$ with its components B_x and B_z.

tor and determines the amplitude of transitions between the Zeeman substates of a nuclear level. The matrix representations of V_e and V_g for ^{57}Fe are

$$V_e = \frac{1}{2}\begin{pmatrix} 3\beta_e & \sqrt{3}\alpha_e & 0 & 0 \\ \sqrt{3}\alpha_e & \beta_e & 2\alpha_e & 0 \\ 0 & 2\alpha_e & -\beta_e & \sqrt{3}\alpha_e \\ 0 & 0 & \sqrt{3}\alpha_e & -3\beta_e \end{pmatrix} \tag{7}$$

and

$$V_g = \frac{1}{2}\begin{pmatrix} \beta_g & \alpha_g \\ \alpha_g & -\beta_g \end{pmatrix}. \tag{8}$$

Amplitudes of the rf field components are again given in Teslas, and all interaction matrix elements are in units of angular frequency, as in Eqs. (2) and (3).

The density matrix of the system describes the nuclear level populations and the transition probabilities between the various energy levels.[26] The density matrix of the ^{57}Fe nucleus has the form

$$\rho = \begin{pmatrix} \rho_{ee} & \rho_{eg} \\ \rho_{ge} & \rho_{gg} \end{pmatrix}, \tag{9}$$

where the four components are block matrices corresponding to the component matrices of the Hamiltonian. Salkola and Stenholm have shown[15] that Mössbauer absorption can be calculated from the density matrix of the system,

$$\mathcal{A} \propto -\mathrm{Im}[\mathrm{Tr}(\mathcal{D}^\dagger \rho_{eg})], \tag{10}$$

where ρ_{eg} is the off-diagonal part of the density matrix. This part of the density matrix can be calculated if we assume that essentially all nuclei are in the ground state. This assumption is valid in Mössbauer spectroscopy, when a spontaneously decaying radiation source is used. The intensity of γ radiation is so small that the system interacts with only one γ photon at a time. In other words, intensity is the highest-order correlation function of γ radiation that can be seen in Mössbauer spectroscopy and Mössbauer $\gamma - \gamma$ correlations can be neglected. In this case $\rho_{ee} \approx 0$ and $\rho_{gg} \approx 1$. The time development of the density matrix can be calculated from the equation of motion

$$i\hbar\partial_t \rho = [H, \rho]_- - \frac{i}{2}[\Gamma, \rho]_+, \tag{11}$$

where the second anticommutator term describes relaxation, including spontaneous emission, and Γ is the linewidth of the Mössbauer transitions. It is now possible to write an equation of motion for the off-diagonal part of the density matrix,

$$\begin{aligned} i\hbar\partial_t \rho_{eg} = {} & [H_e + V_e \cos(\omega t + \varphi)]\rho_{eg} \\ & -\rho_{eg}[H_g + V_g \cos(\omega t + \varphi)] \\ & +\mathcal{D}\rho_{gg} - \frac{i}{2}\Gamma\rho_{eg} - \frac{i}{2}\rho_{eg}\Gamma, \end{aligned} \tag{12}$$

where φ is the phase of the rf field. We are interested in a steady-state solution of the problem and do not consider transient (or pulsed) rf fields. The solution can be written in the form of a Fourier series[9]

$$\rho_{eg} = \sum_{k=-\infty}^{\infty} \rho_{eg}(k) e^{ik(\omega t+\varphi)}. \tag{13}$$

The components of the 4×2 Fourier coefficient matrices $\rho_{eg}(k)$ are further rearranged into a one-dimensional vector according to the rule

$$R(k)_{4(j-1)+i} = [\rho_{eg}(k)]_{ij} \quad (i = 1, ..., 4,\ j = 1, 2). \tag{14}$$

The component matrices of the Hamiltonian must also be rewritten as their supermatrix counterparts, defined by

$$\begin{aligned} \mathbf{H} &= \mathbf{1}_{2\times 2} \otimes H_e - H_g \otimes \mathbf{1}_{4\times 4}, \\ \mathbf{V} &= \mathbf{1}_{2\times 2} \otimes V_e - V_g \otimes \mathbf{1}_{4\times 4}. \end{aligned} \tag{15}$$

The notation $\mathbf{1}_{2\times 2}$ and $\mathbf{1}_{4\times 4}$ is used for unit matrices of indicated dimensions and the $\otimes$ operator is defined by

$$A \otimes B = \begin{pmatrix} a_{11}B & a_{12}B & \cdots & a_{1m}B \\ a_{21}B & a_{22}B & \cdots & a_{2m}B \\ \vdots & \vdots & \ddots & \vdots \\ a_{m1}B & a_{m2}B & \cdots & a_{mm}B \end{pmatrix}. \tag{16}$$

A product of an $m \times m$ and an $n \times n$ matrix gives an $mn \times mn$ matrix. The new $\mathbf{H}$ and $\mathbf{V}$ supermatrices are thus 8×8 complex matrices.

It is now possible to substitute Eq. (13) into Eq. (12), using $R(k)$ in the place of $\rho_{eg}(k)$, and rewrite Eq. (12) for a single k value, omitting the $e^{ik(\omega t+\varphi)}$ factor. This gives a recursion relation for $R(k)$

$$R(k) + \mathbf{A}(k)[R(k+1) + R(k-1)] = -\mathbf{L}(0)\mathbf{D}\delta_{k,0}, \tag{17}$$

where $\mathbf{D}$ is a one-dimensional vector, constructed from the elements of the $\mathcal{D}$ matrix using the same rule that was used for $R(k)$ [Eq. (14)]. The actual form of the $\mathbf{D}$ matrix is not important at this stage, because in the final calculations only products of two $\mathbf{D}$ matrices are needed. The products are given by the matrix $\mathbf{T}$, defined in Eq. (4). The matrices $\mathbf{A}(k)$ and $\mathbf{L}(k)$ are defined as

$$\begin{aligned} \mathbf{A}(k) &= \frac{1}{2}\mathbf{L}(k)\mathbf{V}, \\ \mathbf{L}(k) &= \frac{1}{k\omega + \mathbf{H} - i\gamma}. \end{aligned} \tag{18}$$

The HWHM linewidth of Mössbauer transitions is given by $\gamma = \Gamma/2$. This recursion relation can be solved using the method of matrix continued fractions,[11] by defining matrices $\mathbf{L}_\pm(k)$ as

$$\begin{aligned} R(k) &= \mathbf{L}_+(k)R(k-1), \\ R(k) &= \mathbf{L}_-(k)R(k+1). \end{aligned} \tag{19}$$

In this case $R(0) = \mathbf{GD}$, with

$$\mathbf{G} = -\frac{1}{1 + \mathbf{A}(0)[\mathbf{L}_+(1) + \mathbf{L}_-(-1)]}\mathbf{L}(0). \tag{20}$$

The $\mathbf{L}_{\pm}(k)$ matrices can be obtained by substituting the first or the second line of Eq. (19) into Eq. (17), giving

$$\mathbf{L}_{\pm}(k) = -\frac{1}{1+\mathbf{A}(k)\mathbf{L}_{\pm}(k\pm 1)}\mathbf{A}(k). \tag{21}$$

When calculating the Mössbauer spectrum as a function of energy, we only need the time average of absorption over the rf field period, and thus only $\rho_{eg}(0)$ in Eq. (13) is needed. Substituting $R(0)$ into Eq. (10), in the place of ρ_{eg}, gives the time-averaged absorption

$$\mathcal{A} = -\mathrm{Im}[\mathbf{D}^{\dagger}\mathbf{G}\mathbf{D}] = -\mathrm{Im}\sum_{i,j}\mathbf{G}_{ij}\mathbf{T}_{ij}. \tag{22}$$

Finally, the time dependence of absorption can be calculated by using Eq. (19) and Eq. (13). Only even harmonics need to be summed due to symmetry reasons, absorption does not depend on the sign of the rf field. This gives the time-dependent density matrix $\rho_{eg}(t)$, which can be substituted into Eq. (10). The final expression for the time-dependent absorption is

$$\begin{aligned}\mathcal{A}(t) = &-\mathrm{Im}\sum_{\substack{k>0\\ i,j}}\mathbf{G}_{+}(2k)_{ij}\mathbf{T}_{ij}e^{i2k(\omega t+\varphi)}\\ &-\mathrm{Im}\sum_{i,j}\mathbf{G}_{ij}\mathbf{T}_{ij}\\ &-\mathrm{Im}\sum_{\substack{k<0\\ i,j}}\mathbf{G}_{-}(2k)_{ij}\mathbf{T}_{ij}e^{i2k(\omega t+\varphi)},\end{aligned} \tag{23}$$

where

$$\mathbf{G}_{\pm}(k) = \mathbf{L}_{\pm}(k)\mathbf{L}_{\pm}(k\mp 1)\cdots\mathbf{L}_{\pm}(\pm 1)\mathbf{G}. \tag{24}$$

In practical calculations a maximum absolute value $k_{\max}$ is chosen for k in Eqs. (21) and (23). It is assumed that $\mathbf{L}_{\pm}(k_{\max}\pm 1) = 0$, and $\mathbf{L}_{\pm}(k_{\max}) = \mathbf{A}(k_{\max})$. The choice of $k_{\max}$ depends on the amplitude and frequency of the rf field. The number of terms required in case of a very strong rf field $B_x = B_z = 20$ T at various frequencies is shown in Fig. 2. The two curves correspond to relative errors of 10^{-3} and 10^{-6} in the computed absorption values if $k_{\max}$ is incremented. Calculations start by computing, and possibly storing, the 8×8 complex matrices $\mathbf{L}_{\pm}(k)$, starting from $\mathbf{L}_{\pm}(\pm k_{\max})$, and finishing with $\mathbf{L}_{\pm}(\pm 1)$. It is then possible to calculate the $\mathbf{G}$ matrix and from that the actual time-averaged absorption, using Eq. (22). This process is repeated for each point in the Mössbauer spectrum, substituting the corresponding Doppler velocity into Δ_0 in Eq. (2).

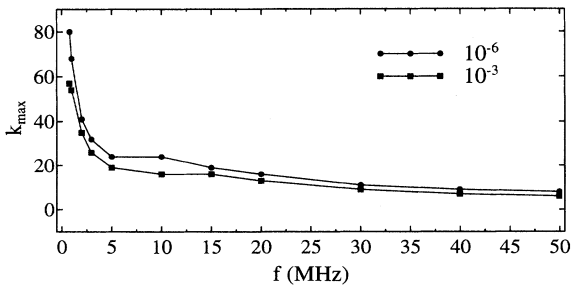

FIG. 2. The maximum number of continued fraction terms that need to be calculated to obtain a relative error below 10^{-3} or 10^{-6} in the computed absorption values for different frequencies of the rf field.

Time-dependent absorption is calculated in the same way, except that the intermediate $\mathbf{L}_{\pm}(k)$ values should be stored and used for calculating the $\mathbf{G}_{\pm}(k)$ matrices according to Eq. (24). These matrices are then used in Eq. (23), giving the actual time development. The angular frequency of the rf field is given by ω, and φ is the initial phase of the external field.

It can be seen in Fig. 2 that the continued fractions converge quickly in the range of the excited and ground state resonance frequencies (20–40 MHz). When the frequency drops below the natural linewidth, the number of terms in the $\mathbf{L}_{\pm}(k)$ matrix recursion increases rapidly and the continued fraction method in the present form becomes computationally inefficient. In practical calculations most of the time is spent on matrix inversion [Eq. (21)]. In that case it is possible to move the time dependence from the density matrix into the state vectors, using the Floquet state expansion.[27,28]

A. Energy domain

The influence of a resonant magnetic field can be seen in Fig. 3. The static field is B_0=28 T and the corre-

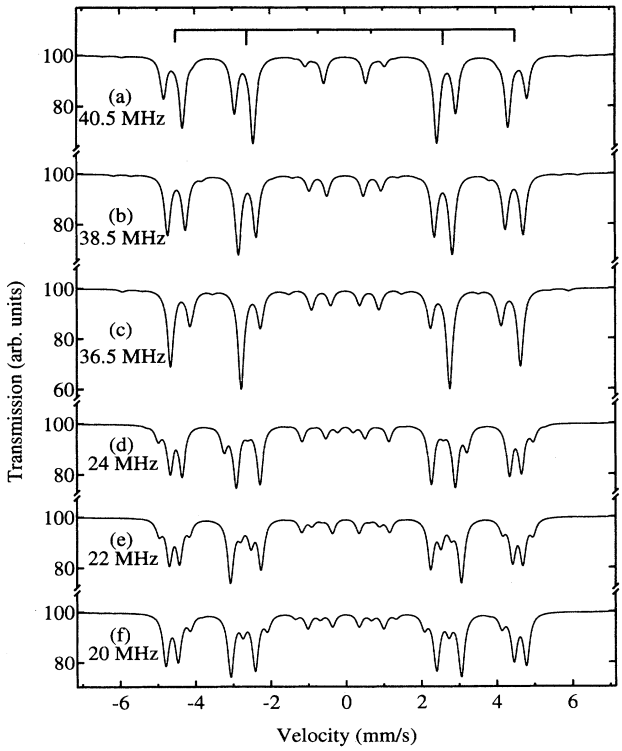

FIG. 3. The calculated splitting of Mössbauer absorption lines of ^{57}Fe due to rf magnetic modulation. The original absorption lines are shown at the top of the figure. The static field is 28 T and the perpendicular rf field amplitude is 8 T. The linewidth is equal to the natural linewidth. Modulation frequencies are shown for each spectrum.

sponding ground state and excited state resonance frequencies are 38.5 MHz and 22 MHz, respectively. The rf field amplitude is 8 T and it is perpendicular both to the static field and to the direction of γ ray propagation ($\phi = \theta = 90°$). The positions of the absorption lines in the original six-line spectrum are shown at the top of the figure. The linewidth γ has been set equal to the natural linewidth of $\Gamma_0 = 0.095$ mm/s.

Splitting of the absorption lines is clearly visible. Each line splits into $2j + 1$ components, where j is the spin of the nuclear state with which the rf field is in resonance. In case of ^{57}Fe this means splitting into two components at the ground state resonance and into four components at the excited state resonance. In contrast to the RWA results,[4] the splitting is asymmetric even at resonance [Figs. 3(b) and 3(e)]. As the frequency is varied slightly below or above resonance, the relative amplitudes of the components change. The components with larger absolute energies have smaller amplitudes above the resonance frequency [Fig. 3(a)], and larger amplitudes below the resonance frequency [Fig. 3(c)]. The same applies in case of the excited state resonance [Figs. 3(d) and 3(f)], but the changes are not as clear, because the various components tend to overlap, particularly at lower rf field amplitudes.

It has been shown previously that direct magnetic modulation can produce sidebands in a Mössbauer spectrum.[22,29] This effect can be seen in ^{57}Fe spectra if the amplitude of the rf field is large. The positive velocity part of an ^{57}Fe spectrum is plotted in Fig. 4. The positions of the original absorption lines are indicated at the top of the figure. The static field is again B_0=28 T and the amplitude of the rf field is 12 T. The modulation frequency is 38.5 MHz, corresponding to the ground state resonance frequency. The effect of a longitudinal field is illustrated in Fig. 4(a). Sidebands appear and they are displaced from the parent lines by $\pm\hbar\omega$. The amplitudes are proportional to the components of the interaction matrix $\mathbf{V}$, and thus also to the spins of the states that are involved in a particular parent transition. As can be seen in Fig. 4(a), the sideband caused by the $1/2 \rightarrow 1/2$ transition at 5.9 mm/s is smaller than the sideband of the $3/2 \rightarrow 1/2$ transition at 7.8 mm/s. Smaller sidebands are also created by a transverse field [Fig. 4(b)]. The effect of simultaneous transverse and longitudinal fields can be seen in Fig. 4(c).

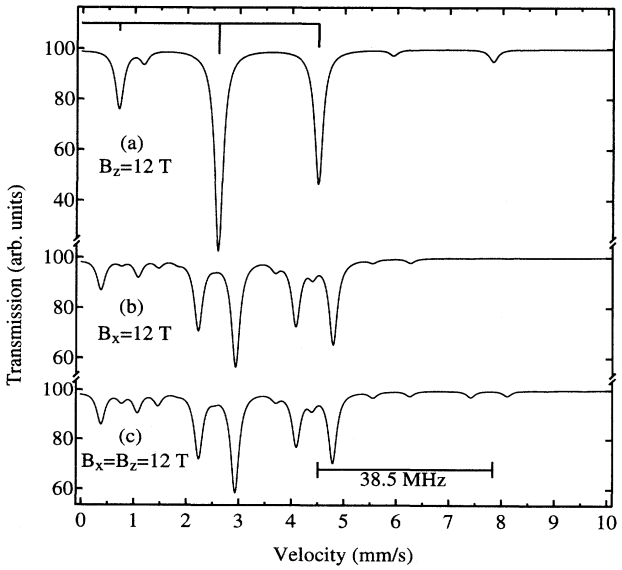

FIG. 4. Calculated sidebands caused by a 12 T rf field. The static field is 28 T and the modulation frequency is 38.5 MHz. In (a) the rf field is parallel with the static field, in (b) it is perpendicular to the static field, and both components are present in (c).

Line splitting decreases rapidly as the modulation frequency drops below the excited state resonance, but absorption lines are shifted from their unperturbed positions. This effect was first analyzed by Bloch and Siegert[13] using perturbation calculation. They interpreted the shift to be caused by the counter-rotating component of the linear rf field. In the rotating wave approximation this component is ignored and line shifts are not present. Bloch and Siegert showed that the shift is essentially proportional to B_{rf}^2 and this has also been observed by Autler and Townes.[12] The effect has been later analyzed using Floquet theory[14] and matrix continued fractions.[9,11]

The possibility of observing this shift depends strongly on the experimental linewidth. A 10 T perpendicular rf field at 7 MHz would cause a shift of $2\Gamma_0$ in the positions of the outer absorption lines if the static field strength is B_0=28 T.

B. Time domain

In addition to the conventional energy domain measurements, it is also possible to study the absorption as a function of time at a constant energy. A constant velocity drive would be used to shift the Mössbauer source radiation energy to coincide with a desired absorption line in the energy spectrum. Such time domain experiments are particularly useful at low frequencies, close to the natural linewidth (1.128 MHz for ^{57}Fe). In this frequency range, changes in a usual velocity scan would at best be seen as line broadening. Time domain measurements, however, still allow the influence of the magnetic modulation to be studied in detail. The two spectroscopic modalities also probe different magnetic response mechanisms in the sample. Time domain measurements require a coherent response from the absorber to the external magnetic field. Phase differences as a function of depth or position in the sample quickly reduce the observable effect. Energy domain measurements do not have such a requirement, and line splitting would be observed even if there is a phase shift between the oscillations of the local field in different parts of the absorber.

The influence of a transverse rf field on the time dependence of Mössbauer absorption can be seen in the spectrochronogram of Fig. 5. Absorption is plotted as a function of the rf field phase at various constant velocities. The static field is 28 T and the amplitude of the transverse rf field is 8 T. Modulation frequency is 1.5 MHz.

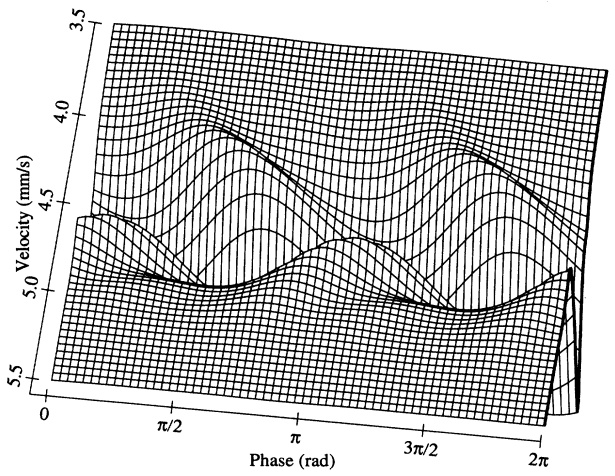

FIG. 5. A spectrochronogram showing the effect of an 8 T transverse field close to the $3/2 \rightarrow 1/2$ transition. Modulation frequency is 1.5 MHz, and the static field is 28 T.

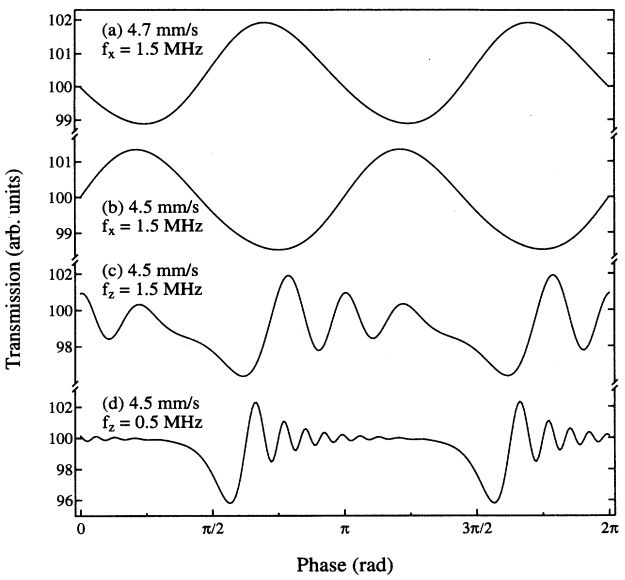

FIG. 6. The calculated time dependence of Mössbauer absorption close to the $3/2 \rightarrow 1/2$ transition in a 28 T static field. The plots show the influence of a 1.5 MHz transverse field (f_x) at 4.7 mm/s (a) and 4.5 mm/s (b). The effect of a longitudinal field (f_z) at 4.5 mm/s is shown in (c) and (d). The modulation frequency is 1.5 MHz in (c), and 0.5 MHz in (d). The rf field amplitude is 8 T in all plots.

Under transverse modulation at low frequencies the elements of the $\mathbf{L}_{\pm}(k)$ matrices are small and consequently only the $k = 0$ and $\pm 2\omega t$ terms have a significant amplitude in Eq. (23). Due to this, the time dependence is dominated by the second harmonic. The phase of the signal is strongly dependent on the detuning from a specific resonance line. A 28 T hyperfine field places the outermost absorption lines of ^{57}Fe at ± 4.6 mm/s. The spectrochronogram in Fig. 5 shows the time-dependent absorption close to this resonance line. It can be seen that higher harmonics begin to appear as the detuning from resonance is increased. The phase of the second harmonic shifts by almost $\pi/2$ as the detuning from resonance (the Doppler shift) is increased from 4.6 mm/s to 5.5 mm/s. The most easily observable effect is, however, the $\pi/2$ phase step, which occurs when the resonance is crossed. This can be seen in Fig. 5 by comparing the absorption signal on the opposite slopes of the absorption line.

The $\pi/2$ phase step can be seen more easily in Figs. 6(a) and 6(b), where two time dependencies have been extracted from Fig. 5. The Doppler shift [Δ_0 in Eq. (2)] is 4.7 mm/s in Fig. 6(a), and 4.5 mm/s in Fig. 6(b). Both plots show slightly asymmetric second harmonics, and the $\pi/2$ phase change is clearly visible.

A longitudinal field of the same magnitude and frequency has an even more dramatic effect [Fig. 6(c)]. The Doppler shift is 4.5 mm/s. In Fig. 6(d) the modulation frequency has been reduced to 0.5 MHz. Longitudinal modulation only affects the diagonal elements of the Hamiltonian, shifting the positions of the absorption lines. At 0.5 MHz, wiggles typical of a fast sweep over a resonance, can be seen. Time dependencies of this type have been observed in ^{67}Zn experiments.[29,30]

III. EXPERIMENT

All experiments were performed in transmission geometry. The energy domain measurements were made with a ^{57}Co:*Pd* source (activity $\approx$1.6 mCi), using a linear velocity scale. A 25 mCi ^{57}Co:*Rh* source was used in the time domain experiments. The sample was a 6 mm $\times$ 6 mm $\times$ 2.5 μm thick FeNi foil, containing 18.02% iron, enriched to 92.8% ^{57}Fe. The foil was mounted inside an acrylic sample holder which allowed the sample to be cooled by water on one side.[31] A water flow rate of 1.5 cm^3/s was sufficient to prevent heating of the sample. The sample holder was situated inside the rf coil. The coil was made of 0.8 mm CuNi tubing, and was also water cooled. It was part of a rf resonance circuit which was tuned for each measurement so that practically all rf energy was absorbed in the coil. In energy domain measurements the resonance circuit was fed by a rf amplifier capable of delivering up to 20 W of power, producing a magnetic field of the order of 1 mT inside the rf coil. The rf power was switched on and off at 1 s intervals to prevent heating of the components of the circuit, and to accumulate a reference spectrum during each measurement.

A modified setup, which allowed the absorption to be studied at a specific γ ray energy as a function of the rf field phase, was used for the time-domain measurements. A constant velocity drive was used to shift the source radiation energy so that it coincided with one of the six absorption lines of the absorber. A time to amplitude converter (TAC) was used to measure the time intervals between the arrival of γ rays in the photomultiplier and trigger pulses from the rf generator. Pulses from the photomultiplier anode were amplified with a fast preamplifier and time pickoff was accomplished with a constant fraction discriminator. Pulses from the last

dynode were amplified with a spectroscopy amplifier and the 14.4 keV radiation was selected with a single channel analyzer, gating the TAC. The trigger pulse frequency from the rf generator was divided by four, so that absorption during four consecutive rf field periods could be measured. A pulse rate of 3 kHz could be achieved at the TAC output. In time domain measurements the rf generator was gated by the Mössbauer drive function generator, so that the rf power was switched on only for the period when the Mössbauer drive was maintaining the desired constant velocity. This reduced the heating problems in the sample and the coil. Maximum power level in these experiments was $\approx 60\ W$.

IV. RESULTS AND DISCUSSION

A reference spectrum of the FeNi sample is shown in Fig. 7. The lines are broadened due to an intrinsic distribution of hyperfine fields in the sample. The line intensities indicate that the angle between the γ rays and the direction of the hyperfine field is close to 70°. The foil is thus magnetized along the direction of easy magnetization closest to the foil surface.

The FeNi alloy forms a fcc lattice, where iron is uniformly distributed in a solid solution, and each iron atom has 12 nearest neighbors. The broadening can be analyzed by assuming a linear dependence between the hyperfine field and the number of Fe nearest neighbors for each iron atom.[32,33] The magnetic field at an iron nucleus with n Fe-Fe nearest neighbors is

$$B_n = B_L + nB_T, \tag{25}$$

where B_L is the local field and B_T is the transferred field. The probability of finding n Fe nearest neighbors can be calculated from the binomial distribution

$$P_n = \frac{12!}{n!(12-n)!}x^n(1-x)^{12-n}, \quad n = 0 \ldots 12, \tag{26}$$

where x is the iron concentration in the alloy. Analysis of the spectrum showed that only the six largest components ($n = 0 \ldots 5$) needed to be used in the fit. The fit in Fig. 7 was obtained with the values of B_L=25.97(8) T and B_T=1.01(3) T. The maximum of the distribution was at 28 T. The six largest components and their relative amplitudes are plotted at the top of the figure. Possible effects of isomer shift changes, and variation of quadrupole constants between the hyperfine components, are known to be small in Fe-Ni alloys with small concentrations of iron[34] and were neglected.

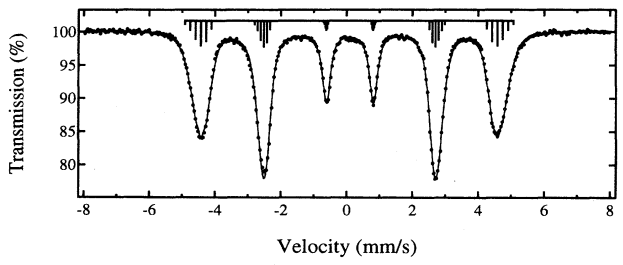

FIG. 7. Mössbauer spectrum of the FeNi foil. The six components used in the fit are shown at the top of the figure. Relative amplitudes were calculated from the binomial distribution.

The resonance frequencies corresponding to the largest component with $B_0 = 28$ T are 38.5 MHz for the excited state and 22 MHz for the ground state. The effect of a rf magnetic field close to the ground state resonance frequency can be seen in Fig. 8. The rf power absorbed by the LC resonance circuit was 11 W for spectrum (a) and 15 W for spectra (b) and (c), producing a field of $\approx 10^{-3}$ T. The splitting is not fully resolved due to the relatively large linewidth caused by the hyperfine field distribution. Higher field amplitude allowed the splitting to be increased, but also induced mechanical vibrations in the sample and caused acoustic sidebands to appear in the spectra.

The spectra shown in Fig. 8 can be compared with the plots in Figs. 3(a)–3(c). It can be seen that above the resonance frequency [Fig. 8(a)] the outer component of each split line is smaller, while at or below the resonance frequency [Figs. 8(b) and 8(c)] the inner components are smaller.

Three largest hyperfine components were selected for the fit. Each component was assigned a static field value according to Eq. (25). The relative amplitudes of the components were calculated from Eq. (26). Different amplitudes of the transverse and longitudinal rf fields were assigned to each hyperfine component according to the assumption that they have a linear dependence on the static hyperfine field. The fitting results are given in Table I. It can be seen that the rf field causes the av-

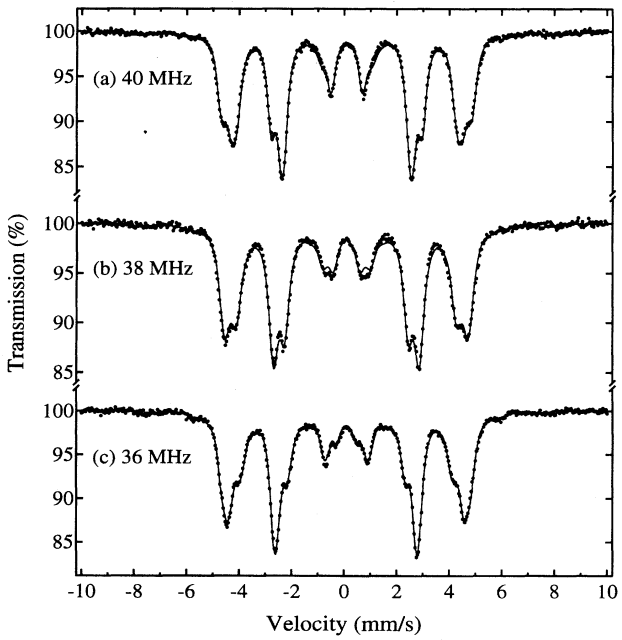

FIG. 8. Double resonance spectra measured at frequencies close to the ground state resonance. The frequencies are 40 MHz (a), 38 MHz (b), and 36 MHz (c).

TABLE I. Fitting results of the rf modulation experiments showing the rf field frequency, power level, center of the hyperfine field distribution B_c and the maximum values of the transverse ($B_{x,\max}$) and longitudinal ($B_{z,\max}$) rf field components.

f (MHz)	Power (W)	B_c (T)	$B_{x,\max}$ (T)	$B_{z,\max}$ (T)
40	11	27.8	6.4	7.8
38	15	27.7	7.0	7.3
36	15	27.8	8.2	8.9
30	18	26.4	21.2	18.0
27	10	27.1	11.7	12.2
24	15	26.6	15.1	7.8
19	15	26.6	15.8	9.4
1.45	38	27.4	10.8	1.4
0		28.0		

erage hyperfine field at the nucleus to decrease slightly. The maximum values of the transverse and longitudinal field amplitudes are almost of the same magnitude when the modulation frequency is above 30 MHz. The hyperfine components with larger static field values appear to have smaller values for the transverse field amplitude and larger values for the longitudinal field amplitudes.

The spectrum in Fig. 8(b) was measured closest to the resonance frequency of the ground state ($\approx$ 38.5 MHz). The splitting of absorption lines, caused by the rf field, is clearly visible. The effect of the longitudinal modulation is demonstrated in Fig. 8(c) as small absorption lines at $\pm$5.5 mm/s. The fit of the spectra in Fig. 8 indicated that the longitudinal field amplitude was between 3 T and 9 T for all components.

At lower frequencies the rf field couples to both the excited state and the ground state of an ^{57}Fe nucleus. A spectrum measured at 30 MHz is shown in Fig. 9(a). This frequency is between the resonance frequencies of 38.5 MHz and 22 MHz. The splitting becomes more complex and cannot be fully resolved due to the distribution of hyperfine fields in the FeNi foil. A good fit can, however, be achieved by using the six largest hyperfine components with relative amplitudes again derived from the binomial distribution of Eq. (26).

The spectra in Figs. 9(b)–9(d) show the effect of the rf field as the frequency is scanned over the excited state resonance. The splitting is not fully resolved, but the change in the spectra above and below the resonance frequency can be seen most clearly in Figs. 9(c) and 9(d) at around $\pm$3 mm/s. The intensity redistribution can be compared to the simulations in Figs. 3(d)–3(f).

As can be seen from Table I, the average static field at the Fe nuclei has decreased from the unperturbed value by $\approx$1.5 T. The decrease is larger than it was in the case of the ground state resonance, and is accompanied by a considerable increase of the $B_{x,\max}$ and $B_{z,\max}$ values. The decrease of B_c from the unperturbed value also appears to correlate with the power levels used in the measurements. The largest B_x and B_z amplitudes are associated with the components having the smallest hyperfine fields (in the range 22–24 T), and decrease to nearly zero for the hyperfine components having the largest static field (in the range 28–29 T).

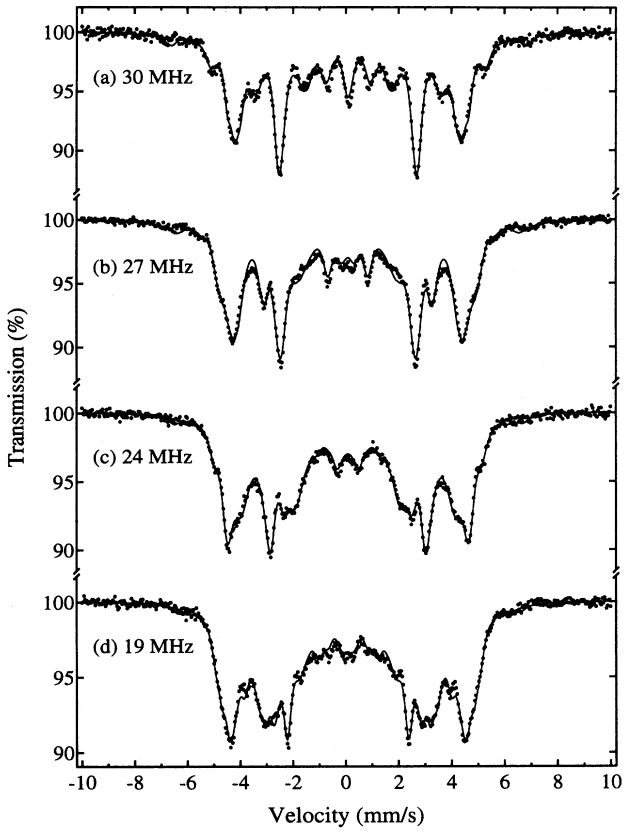

FIG. 9. Double resonance spectra measured at frequencies close to the excited state resonance. The frequencies are (a) 30 MHz, (b) 27 MHz, (c) 24 MHz, and (d) 19 MHz.

The fitting results indicate that the external rf field does not exceed the anisotropy field in the foil and cannot reverse the direction of the internal magnetization. It can, however, turn the internal field by a certain angle. The results in Table I indicate that angles of up to 60° can be observed. The rotation angle is smaller for the hyperfine components with larger static fields.

As the modulation frequency is reduced, the splitting of lines also decreases. When the frequency is close to the natural linewidth, splitting can no longer be observed. The only visible effect in a conventional velocity scan is a slight broadening of absorption lines. This can be seen in Fig. 10(a), where the modulation frequency is 1.45 MHz. The unperturbed reference spectrum is shown with a dashed line. In this case, however, it is possible to study the time dependence of absorption. The results in Figs. 10(b) and 10(c) were measured at constant velocities of 4.9 mm/s and 4.1 mm/s, correspondingly. These positions are shown with arrows in Fig. 10(a).

In these experiments, the rf magnetic field has a relatively large transverse component and a small longitudinal component. This means that the dominating feature in the time dependence of absorption is the second harmonic, as can be seen in Figs. 10(b) and 10(c). Both the amplitude and the phase of the absorption signal are strongly dependent on the constant velocity, i.e. detuning from resonance. The $\pi/2$ phase shift visible between

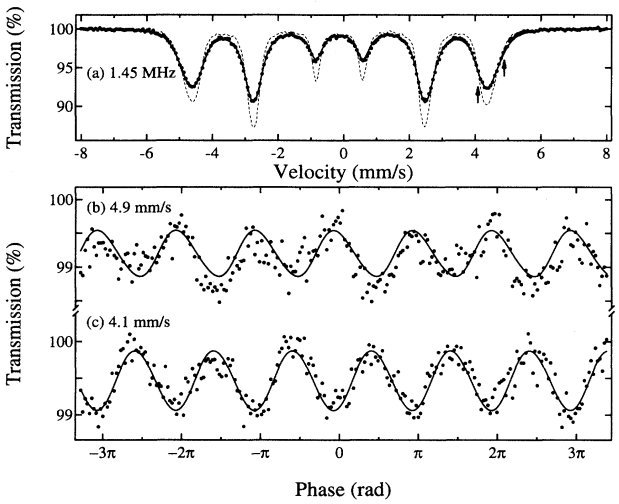

FIG. 10. A velocity scan measured at the modulation frequency of 1.45 MHz (a). Arrows mark the constant velocities used in time-domain measurements, the dashed line shows the unperturbed reference spectrum. The time dependence of absorption at the constant velocity of 4.9 mm/s is shown in (b), and at 4.1 mm/s in (c).

the signals in Fig. 10(b) and Fig. 10(c) is due to the fact that the constant velocities were chosen to be on the opposite slopes of the outermost absorption line at 4.6 mm/s. This can be compared with the theoretical predictions in Figs. 6(a) and 6(b).

Fitting of the spectrum in Fig. 10(a) gave a value of 10(2) T for the amplitude of the transverse rf field. Fitting of the time-dependencies gave a smaller value of 5(1) T. Both fits indicated only a negligible longitudinal field amplitude, as shown in Table I.

The amplitude of the absorption signal at 1.45 MHz was of the order of 1%. Time domain measurements were also attempted at higher frequencies. The amplitude of the time-dependent absorption was found to decrease rapidly as the frequency was increased. At 2.3 MHz, no time-dependent signal could be observed, indicating that the FeNi foil no longer had a coherent response to the external rf field.

V. CONCLUSIONS

We have measured Mössbauer-NMR double resonance spectra of a thin FeNi foil. It was possible to achieve strong rf magnetic fields at the Fe nucleus by means of ferromagnetic enhancement of a relatively weak external field (≈ 1 mT). Radio-frequency field amplitudes at the nucleus of up to 20 T were observed. Proper mounting of the sample foil was found to be an effective way of dissipating acoustic vibrations caused by the magnetostrictive properties of the ferromagnetic sample, and enabled the measurement of double resonance spectra, which were free of acoustic sidebands.

The presence of an intrinsic distribution of hyperfine fields in the FeNi alloy made it difficult to observe the full details of line splitting at frequencies close to the excited state resonance. Another limiting factor was the maximum achievable rf field amplitude. It would be advantageous to use a different absorber with a smaller linewidth. Our work has indicated that a material with a larger coefficient of magnetostriction could probably be used, provided that proper mounting of the sample foil is maintained.

We have also studied the time dependence of the Mössbauer absorption. This method has proven to be usable at low frequencies, close to the natural linewidth of ^{57}Fe. In this frequency range the conventional energy domain spectrum was only slightly affected. In time domain, however, dramatic effects were observed. The oscillation of absorption as a function of the rf field phase should be observable even in the presence of mechanical vibrations in the sample because the mechanical vibrations are incoherent and would be averaged out in the time dependence. Time domain measurements were found to be more sensitive to a rf field which is parallel with the static field. The effects of a perpendicular field were more pronounced in a traditional velocity scan.

All experimental results were successfully analyzed using the density matrix description of the nuclear system. The theory allowed us to analyze both energy and time domain results. The frequency range where the theory is applicable is very wide, with the lower limit being set by the natural linewidth. Below that limit the matrix continued fractions converge very slowly. There are no convergence problems above 20 MHz, in the range of the nuclear resonance frequencies.

ACKNOWLEDGMENTS

The authors thank Professor S. Stenholm, Professor J. Javanainen, and Dr. M. Salkola for fruitful discussions. We thank Professor C. B. Collins from the University of Texas at Dallas for providing the FeNi foils. Financial support from the Academy of Finland, the Jenny and Antti Wihuri Foundation, and the Finnish Cultural Fund is acknowledged.

* Present address: Research Institute for Theoretical Physics, P.O. Box 9, FIN-00014 University of Helsinki, Finland.

[1] I. Tittonen, M. Lippmaa, E. Ikonen, J. Lindén, and T. Katila, Phys. Rev. Lett. **69**, 2815 (1992).
[2] M. N. Hack and M. Hamermesh, Nuovo Cimento **19**, 546 (1961).
[3] A. V. Mitin, Sov. Phys. JETP **25**, 1062 (1967).
[4] H. Gabriel, Phys. Rev. **184**, 359 (1969).
[5] A. V. Mitin, E. F. Makarov, and N. V. Polyakov, Sov. Phys. JETP **63**, 1130 (1986).
[6] S. Olariu, Phys. Rev. B **37**, 7698 (1988).

[7] S. Olariu, T. W. Sinor, and C. B. Collins, Phys. Rev. B **50**, 616 (1994).
[8] J. Odeurs, Hyperfine Interact. **92**, 1043 (1994).
[9] S. Stenholm, J. Phys. B **5**, 878 (1972).
[10] S. Stenholm, J. Phys. B **5**, 890 (1972).
[11] A. Valli and S. Stenholm, Phys. Lett. **64A**, 447 (1978).
[12] S. H. Autler and C. H. Townes, Phys. Rev. **100**, 703 (1955).
[13] F. Bloch and A. Siegert, Phys. Rev. **57**, 522 (1940).
[14] J. H. Shirley, Phys. Rev. **138**, 979 (1965).
[15] M. Salkola and S. Stenholm, Phys. Rev. A **41**, 3838 (1990).
[16] G. J. Perlow, Phys. Rev. **172**, 319 (1968).
[17] E. Matthias, in *Hyperfine Interactions and Nuclear Radiations*, edited by E. Matthias and D. A. Shirley (North-Holland, Amsterdam, 1968), pp. 815–841.
[18] N. D. Heiman, L. Pfeiffer, and J. C. Walker, Phys. Rev. Lett. **21**, 93 (1968).
[19] L. Pfeiffer, in *Mössbauer Effect Methodology*, edited by I. J. Gruverman (Plenum, New York, 1971), Vol. 7, pp. 263–298.
[20] T. W. Sinor, P. W. Reittinger, and C. B. Collins, Phys. Rev. Lett. **62**, 2547 (1989).
[21] S. S. Yakimov *et al.*, JETP Lett. **26**, 13 (1977).
[22] P. J. West and E. Matthias, Z. Phys. A **288**, 369 (1978).
[23] V. K. Voitovetskii, S. M. Cheremisin, and S. B. Sazonov, Phys. Lett. **83A**, 81 (1981).
[24] F. G. Vagizov, Hyperfine Interact. **61**, 1359 (1990).
[25] F. G. Vagizov, Hyperfine Interact. **95**, 85 (1995).
[26] S. Stenholm, *Foundations of Laser Spectroscopy* (Wiley, New York, 1984), p. 17.
[27] I. Tittonen, J. Javanainen, M. Lippmaa, and T. Katila, Hyperfine Interact. **78**, 397 (1993).
[28] I. Tittonen, M. Lippmaa, and J. Javanainen (unpublished).
[29] E. Ikonen, P. Helistö, J. Hietaniemi, and T. Katila, Phys. Rev. Lett. **60**, 643 (1988).
[30] E. Ikonen, J. Hietaniemi, and T. Katila, Phys. Rev. B **38**, 6380 (1988).
[31] M. Lippmaa, I. Tittonen, J. Lindén, and T. Katila, Nucl. Instrum. Methods B **76**, 146 (1993).
[32] D. G. Rancourt and J. Y. Ping, Hyperfine Interact. **69**, 497 (1991).
[33] J. Hesse and J. B. Müller, Solid State Commun. **22**, 637 (1977).
[34] B. Window, J. Phys. F **4**, 329 (1974).